



Precipitation Hardening and Corrosion Behavior of Friction Stir Welded A6005-TiB₂ Nanocomposite

N. Abu-warda¹ · M. D. López¹ · B. González¹ · E. Otero¹ · M. D. Escalera-Rodríguez¹ · S. Cruz² · P. Rey² · D. Verdera² · M. V. Utrilla¹

Received: 17 January 2020 / Accepted: 4 March 2020 / Published online: 25 March 2020
© The Korean Institute of Metals and Materials 2020

Abstract

Precipitation hardening and corrosion behavior of a friction stir welding (FSW) based on the aluminum alloy A6005 reinforced with TiB₂ nanoparticles have been studied. Mechanical alloying (MA) and hot extrusion techniques have been employed as processing route followed by FSW. Samples characterization has been performed by DSC and TEM, and precipitation strengthening of the bulk samples and the FSW joint has been evaluated by micro-hardness tests after T6 thermal treatment. TEM characterization revealed the presence of Mg–Si hardening phases, mainly of β' phase, and dispersoids of α-Al(FeMnCr)Si into the aluminum matrix. The results revealed that samples subjected to MA had less susceptibility to T6 thermal treatment and that the presence of nano-TiB₂ reinforcement accelerates aging time. In addition, electrochemical tests based on polarization tests have been performed in 3.5% NaCl solution to assess the effect of FSW process on corrosion behavior. The FSW joint had worse corrosion behavior since the passive Al₂O₃ film was not generated on the weld zone. SEM–EDS analysis revealed that pits nucleated mainly in sites with a higher presence of Fe contaminant which acts cathodically with respect to the aluminum matrix, producing galvanic corrosion.

Keywords Friction stir welding · Nanocomposite · Titanium diboride · Aluminum · Age-hardening · TEM

1 Introduction

Transport industry and particularly automotive, aerospace and railway industries are demanding materials with high specific properties to develop lightweight structures. This weight reduction is accompanied by a reduction in fuel consumption and CO₂ emissions while optimizing the overall performance. Between these materials, aluminum matrix composites (AMCs) have attracted the attention due to their high specific modulus and strength, and their excellent fatigue and wear behavior [1, 2].

However, the development of AMCs to replace aluminum alloys in the above-mentioned industries needs advanced processing and joining methods. As processing route, MA

allows to obtain optimum powder properties for a posterior consolidation process, as hot extrusion, and it achieves excellent reinforcement distributions [3, 4]. The benefits of MA process were analyzed in detail in a previous study [5]. Otherwise, as joining method, FSW is a solid state welding process with numerous advantages over conventional joining methods based on fusion welding. Many authors [6, 7] determined that the mechanical properties of the welded zone on FSW joints are usually better than the obtained by conventional methods. This improvement is produced because of the solidification induced structure is absent and with that, FSW avoids reinforcement segregation, cracking, distortions in the weld zone and chemical reactions between the aluminum and the reinforcement particles which can form brittle phases.

Heat treatable aluminum 6xxx (Al–Mg–Si) series are used to manufacture extruded components due to their excellent combination of formability and specific strength. FSW joints of these alloys have been widely studied by other researchers [8–10]. According to [11–13], precipitation sequence of these alloys has been approximated to the following sequence: supersaturated solid solution

✉ N. Abu-warda
najib.abuwarda@urjc.es

¹ Dpto. de Matemática Aplicada, Ciencia e Ingeniería de Materiales y Tecnología Electrónica, ESCET, Universidad Rey Juan Carlos, 28933 Móstoles, Madrid, Spain

² AIMEN, Technological Centre, Polígono de Cataboi, E36418 Porriño, Pontevedra, Spain

$\alpha\text{Al} \rightarrow \alpha\text{Al} + \text{clusters of Si and Mg} \rightarrow \alpha\text{Al} + \text{Guinier–Preston (GP) zones} \rightarrow \alpha\text{Al} + \beta'' \rightarrow \alpha\text{Al} + \beta' \rightarrow \alpha\text{Al} + \beta (\text{Mg}_2\text{Si})$. Si and Mg clusters start to form at relatively low temperatures during the heating step and these clusters grow producing more stable GP zones. These GP zones act as stable precursors or cores for the precipitation of β'' . This precipitate ends up forming the precipitate β' and with it the equilibrium phase Mg_2Si . The main hardening phases β' and the equilibrium phase β have the same chemical composition Mg_2Si , with a different crystalline structure. Further to this phase transformation, dispersoids of $\alpha\text{-AlFeSi}$ and $\alpha\text{-Al(Fe,Mn,Cr)Si}$ can be formed as in aluminum alloys, iron is the most common impurity and is usually seen as an intermetallic phase. These dispersoids are 10–500 nm diameter and usually increase resistance to recrystallization and improve fracture toughness [14].

The presence of a ceramic reinforcement into the aluminum matrix has an important effect on the age hardening of AMCs. Precipitation kinetics are usually accelerated with the presence of reinforcement. Rodrigo et al. [15] studied the effect of SiC reinforcement on precipitation kinetics of an AMC and they attributed this behavior to the change in dislocation and vacancies densities in the aluminum matrix.

Salih et al. [16] provided an overview of the state-of-the-art of FSW in aluminum composites and suggested that the maturity of FSW technique in AMCs is still at an early stage in research. There are not many reports that study the precipitation strengthening of FSW on aluminum alloys [17, 18] and, in addition, there are not many reports that evaluate its corrosion resistance [19, 20]. Maggiolino and Schmid [21] evaluated the corrosion behavior of a FSW and a MIG welding of two 6xxx aluminum alloys and they reported that FSW sample had a better behavior concerning pitting corrosion. However, there is a lack of studies which employ electrochemical tests to evaluate corrosion susceptibility of FSW materials.

Thus, the aim of the research is to analyze the effect of the primary processing (MA) and the joining method (FSW) in the thermal treatability and the final properties of an AMC reinforced with nano- TiB_2 particles. In addition, the effect of FSW joining process on corrosion resistance of the AMC has been analyzed by electrochemical tests.

2 Experimental Procedure

2.1 Materials and Processing

A6005 aluminum powders have been used as matrix, while 5 wt% nano- TiB_2 particles have been employed as reinforcement. A detailed description of both matrix powders and nano-reinforcement can be seen in previous studies [5, 22]. A6005 aluminum powder has been firstly consolidated by

hot extrusion and named as “A6005-base”. This sample was used as reference. Two extruded plates “A6005-MA-0%” and “A6005-MA-5%” have been also manufactured to analyze the effect of MA process and the presence of nano- TiB_2 , respectively, on precipitation strengthening of A6005 alloy, Table 1. These samples were MA in a horizontal attritor mill before hot extrusion varying nano- TiB_2 content, from 0 to 5 wt%. The parameters used for MA and extrusion were described in detail in previous studies [5, 23].

The A6005-MA-5% sample has been finally joined by FSW in AIMEN in a PDS-4 Intelligent Stir MTS machine. The tool used was made of H13 (shoulder) and MP159 alloy (pin) and was manufactured by Triton Tooling. The pin was threaded with 3 flutes (length of 2.8 mm and diameter between 4 and 5 mm) and shoulder diameter was 12 mm. The FSW tool was inserted at the interface of the two plates and the welding direction remained parallel to the extrusion direction. The tilt angle of the pin toward the workpiece has been kept constants at 1.5° during the FSW process. Besides, tool rotation speed was 100 rpm (clockwise direction) and the transverse speed remained at 300 mm/min. This sample has been identifying as “A6005-FSW” (Table 1).

2.2 Differential Scanning Calorimetry

DSC analysis is a useful method to design the posterior thermal treatment and to analyze the effect of nano- TiB_2 addition on precipitation kinetic of the A6005 alloy. In this context, DSC has been employed to study the precipitation sequence of the MA and extruded A6005 aluminum alloy. The studied samples were the A6005-MA-0% and the A6005-MA-5% materials. Their preparation for DSC analysis involved grinding the slice obtained from the extruded plates with a 600 grade SiC paper and a subsequent polishing with 3 μm diamond paste. These samples were firstly solution heat treated at 550°C at 1 h in Ar atmosphere, following by water quenching. DSC analysis were carried out in an 822 Mettler Toledo under Ar atmosphere with a $10^\circ\text{C}/\text{min}$ scanning rate. The scans started at 25°C up to 560°C . A relatively slow speed has been used in order to avoid temperature gradients between the inside and outside of the samples. The analyses were performed by placing the sample in the sample pan

Table 1 Manufacturing process and reinforcement content (in wt%) of each sample

Reference name	Manufacturing process	Reinforcement content (wt%)
A6005-base	Extrusion	0
A6005-MA-0%	MA + extrusion	0
A6005-MA-5%	MA + extrusion	5
A6005-FSW	MA + extrusion + FSW	5

and a second scan was performed in order to obtain a baseline. The effects associated with precipitation or dissolution reactions during the heating were obtained by subtracting this baseline. Most interesting results have been extracted from the heating curve. In addition, heat flux differential curve has been plotted against time to determine the inflection points of the curves which mark the beginning and end of the transformations. The tests have been performed by duplicate for each material.

2.3 Precipitation Strengthening

Thermal treatments have been carried out after DSC analysis on A6005-base, A6005-MA-0% and A6005-MA-5% samples to evaluate both MA process and nano-TiB₂ presence, respectively, on precipitation strengthening kinetics. After solution heat treatment (550 °C during 1 h in Ar atmosphere and water quenching), some samples were artificially aged (T6 treatment) at 180 °C during 1, 2, 3, 4, 5, 6, 7, 8, 9 and 10 h. The T6 treatment has been performed in a silicone bath to have precise control of the temperature (180 ± 2 °C). After T6 treatment samples were stored at -5 °C to avoid natural aging. The effect of aging time has been evaluated by micro-hardness tests. For this reason, one side of each sample was ground with a 2400 grade SiC paper before T6 treatment. Micro-hardness of solution heat-treated samples was also measured to use these values as reference.

The precipitation strengthening of A6005-FSW sample has been studied through the analysis of age-hardening curves performed on cross-sections before and after T6 thermal treatment. It was performed at 180 °C during 5 h aging. This time was selected after the optimization of T6 thermal treatment for A6005-MA-5% sample.

2.4 Electrochemical Tests

Electrochemical tests were performed by an Autolab PGSTAT 302 N potentiostat. The analysis has been performed on A6005-MA-5% and A6005-FSW samples, both in T6 condition. The electrolyte test solution was a neutral solution of distilled water containing 3.5 wt% NaCl to simulate the marine environment. Electrochemical measurements were conducted at room temperature (22 °C) in a three-electrode inert polymeric cell. A detailed description of the employed cell and the parameters used for polarization resistance (R_p) and anodic–cathodic polarization measurements can be seen in a previous investigation [22]. The effect of both MA process and nano-TiB₂ addition on corrosion resistance of the A6005 alloy were investigated in [22], and now, the effect of FSW on corrosion behavior has been evaluated.

2.5 Sample Characterization

TEM has been employed to identify nano-TiB₂ reinforcement, Mg–Si precipitates, and α -dispersoids after artificial aging. Discs of 3 mm diameter and 200 μ m thickness have been firstly prepared. These discs were transferred to a focused ion beam, where they reach a thickness of approximately 100 nm. A JEOL JEM 2100 microscope (CNME, Madrid) has been employed for this purpose. The characterization of the different precipitates has been done by means of selected area electron diffraction (SAED) patterns and energy dispersive X-ray spectroscopy (EDX). The microstructure of the FSW joint has been analyzed employing a Leica/DMR optical microscope (OM). In addition, the morphology of pits and corrosion products obtained after electrochemical tests has been identified with a Hitachi S3400N SEM. Semi-quantitative compositional analyses have been carried out using EDX with a Bruker XFlash 5010 detector. Finally, the effect of aging time has been evaluated by micro-hardness tests using a Shimadzu HMV-2 micro-hardness indenter, applying a load of 100 g ($HV_{0.1}$) for 15 s.

3 Results and Discussion

3.1 Base material Characterization

The microstructural characterization of the A6005-MA-5% sample employed for the posterior FSW has been performed in detail in a preliminary study [5]. It has good reinforcement distribution and reduced presence of agglomerates. Good consolidation of nano-TiB₂ particles within the matrix has been achieved. In addition, two phases were identified, one more defined and homogeneously distributed formed mainly by Al and another one more heterogeneously distributed formed by amorphous Al₂O₃ produced during MA stage.

A6005-MA-0% and A6005-MA-5% samples have been analyzed by DSC as Fig. 1 shows. On one hand, A6005-MA-0% sample (Fig. 1a) shown an exothermic peak on heat flow plot for approximately 85 °C (1). This peak is associated with the formation of clusters of Si and Mg. Weng et al. [24] investigated clustering behavior during natural and artificial aging in Al–Mg–Si alloys and they reported that clusters can formed at room temperature or 100 °C. Serizawa et al. [25] concluded that the second clusters, which are formed at 100 °C, can transform continuously into β'' . On the other hand, A6005-MA-5% sample (Fig. 1b) shows two overlapping peaks at that temperature range (1) that would indicate a second precipitation reaction after clustering activities. In both samples, there was also a small exothermic peak that appears for 120 °C (2) related to the formation of GP-I (Guinier–Preston) zones.

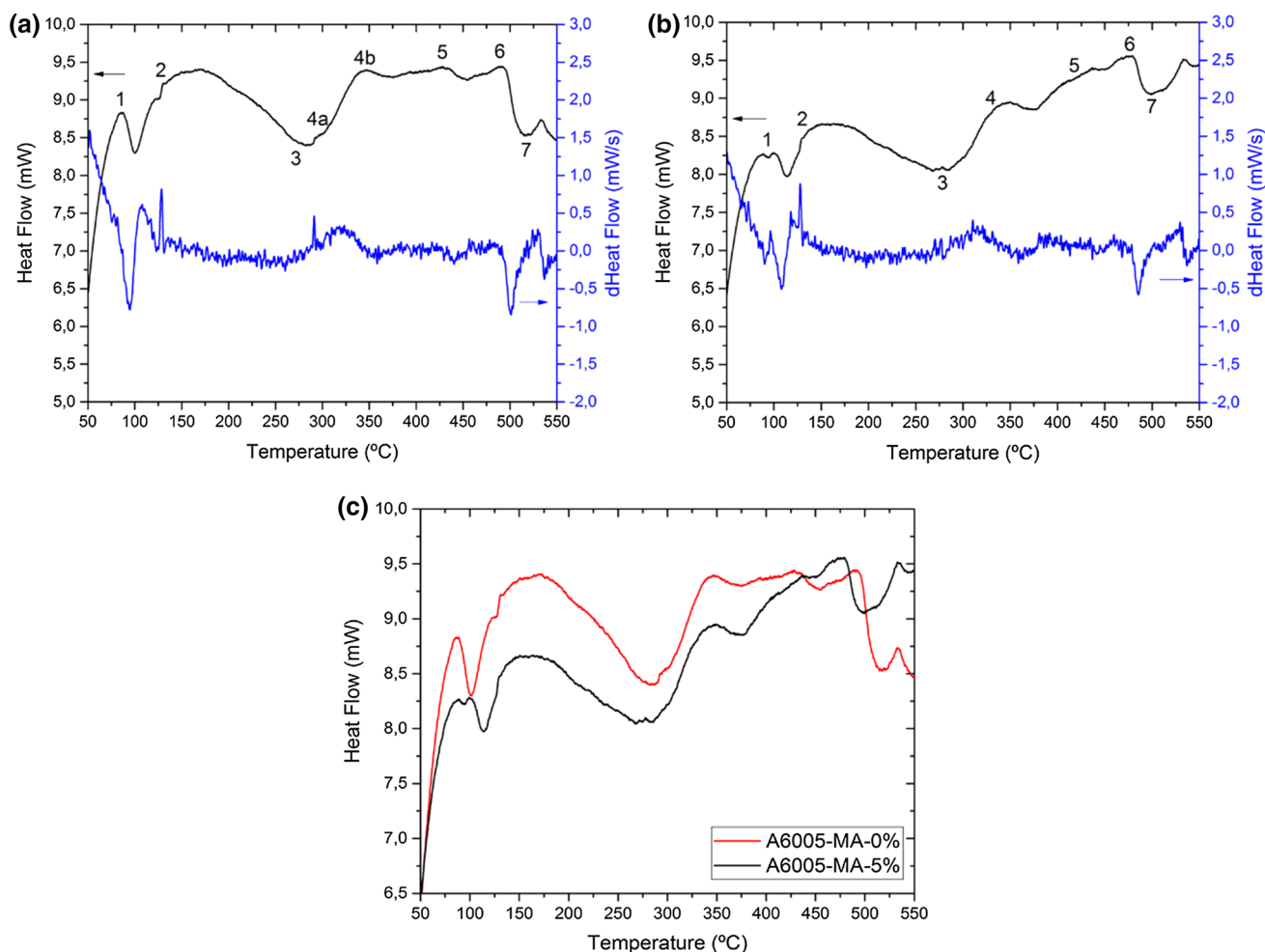


Fig. 1 DSC plots of **a** A6005-MA-0%, **b** A6005-MA-5% and **c** the comparative plot

Marioara et al. [26] investigated the influence of temperature on nucleation of β'' phase in an Al–Mg–Si alloy. They found that GP-I zones are fully coherent pre- β'' particles which were formed from atomic clusters. In addition, for the temperature range between 270 and 290 °C, an endothermic peak related to the dissolution of the clusters (3) has been observed. A6005-MA-0% sample also shown a narrow exothermic peak at 290 °C (4a) and another wider peak (4b). However, on sample A6005-MA-5% only the widest exothermic peak (4), probably associated with the formation of β'' , has been observed. Two other exothermic peaks (5 and 6) have been observed in both samples. These are associated to the transformation of β'' precipitates to β' and β (Mg_2Si), respectively. Finally, a large endothermic peak has been observed (7) in both samples. It is associated with the dissolution of the equilibrium phase. This precipitation sequence is in accordance with the results obtained by Birol [27] for the same A6005 alloy produced without the MA route.

Comparing DSC analysis of both samples (Fig. 1c), in addition to the slight differences observed in peaks (1) and (4), it can be seen that in the reinforced sample heat flow peaks associated with the precipitation of β'' , β' and β appear at lower temperatures compared to the non-reinforced sample. This behavior is justified on the basis that the reinforcement acts as a nucleation site and favors the precipitation of these phases at lower temperature. Rodrigo et al. [15] investigated the effect of SiC reinforcement on precipitation kinetics of A2009 alloy and they confirmed that the presence of reinforcement accelerates the precipitation kinetics of hardening phases.

After DSC analysis, samples were artificially aged at 180 °C at different times to obtain age-hardening curves, Fig. 2. This aging temperature has been selected following ASTM B221 standard. Aging curves of A6005-MA-0% and A6005-MA-5% materials have been used to study the effect of nano-TiB₂ addition on the precipitation strengthening of the A6005 alloy. These curves are quite similar and

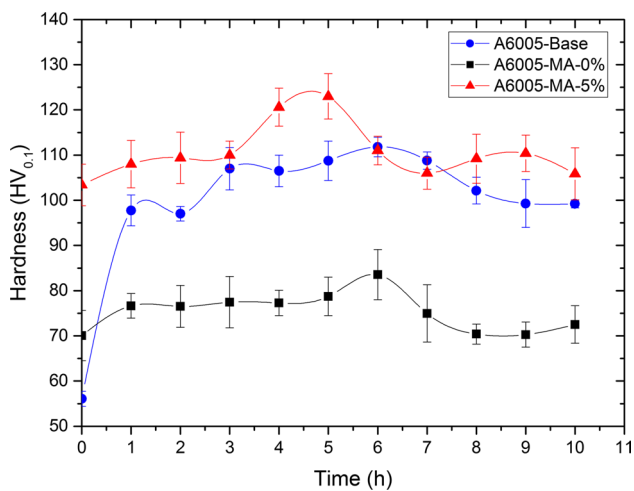


Fig. 2 Age-hardening curves of the A6005 alloy at 180 °C comparing the effect of the MA process and n-TiB₂ reinforcement addition

one predominant hardening peak has been observed in each one. The presence of a ceramic reinforcement as the nano-TiB₂ did not significantly modify the precipitation sequence; however, it accelerates the appearance of the peak-aging. On A6005-MA-5% sample, the maximum hardness peak appears after 5 h of aging while on A6005-MA-0% sample this peak appears after 6 h of aging. These results are in accordance with that obtained on DSC analysis, where the peaks related to the precipitation of β' and β hardening phases appeared at lower temperatures in the reinforced A6005-MA-5% material. Precipitation kinetics are usually influenced by the presence of reinforcement as nano-TiB₂ particles. The reinforcement acts as a preferential nucleation site of the precipitates, which favors and accelerates the precipitation process. In addition, the high deformation generated after quenching from solution temperature, which has been generated by the great difference of thermal expansion coefficients between matrix and reinforcement, produces an increase of dislocation density mainly close to reinforcement particles, as Rodrigo et al. [15] discuss.

Precipitation kinetic is not only influenced by reinforcement presence but also on the processing route. In this context, samples processed by MA have less susceptibility to aging treatment than that A6005-base material. If the age-hardening curve of A6005-base material is compared with those of the materials processed by MA, it undergoes a much more pronounced increase of micro-hardness after 1 h of aging. This may be due to the fact that, as mentioned above, samples processed by MA present two phases, one formed mainly by Al and another one formed by amorphous Al₂O₃ produced during the MA stage. Otherwise, A6005-base sample achieves the maximum micro-hardness after 6 h aging as in A6005-MA-0% sample, this means that the MA process did not accelerate precipitation kinetic.

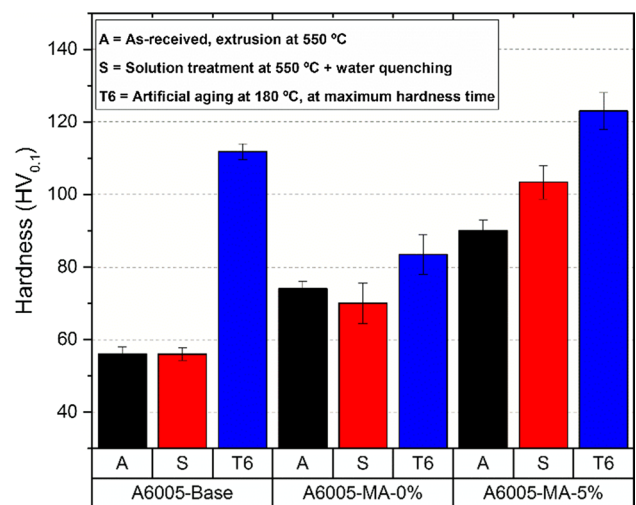


Fig. 3 Micro-hardness evolution of the different materials as function of the thermal treatment

Figure 3 shows micro-hardness evolution of the different materials as function of the thermal treatment. It shows samples micro-hardness (1) after hot-extrusion process, (2) after solution treatment at 550 °C followed by water quenching and (3) after artificial aging for the maximum micro-hardness value (T6 thermal treatment). Comparing the as-received extruded materials, the application of MA supposed an increase of 32% micro-hardness, from 56 HV (A6005-base) to 74 HV (A6005-MA-0%). Otherwise, the addition of nano-TiB₂ reinforcement supposed an increase of 22%, from 74 (A6005-MA-0%) to 90 HV (A6005-MA-5%). The effect of solution treatment on micro-hardness was negligible.

In relation to T6 thermal treatment, the reinforced A6005-MA-5% material increased micro-hardness from 103 HV for the solubilized condition up to 123 HV after T6 treatment (19.4% increase) while the unreinforced A6005-MA-0% material increased from 70 to 83 HV (18.6% increase). The A6005-base material increased micro-hardness from 56 to 112 HV, this supposed an increase of 100%, much higher than that obtained for samples processed by MA. However, it must be noted that micro-hardness increase of A6005-MA-5% sample is permanent because it has been produced by the effect of the new processing route and by the addition of the ceramic particles, while micro-hardness of A6005-base sample could not be maintained during time because it comes mostly from the thermal treatment. A6005-base sample is more susceptible to undergo natural overaging than A6005-MA-5% sample.

After T6 thermal treatment A6005-base and A6005-MA-5% samples were microstructurally characterized by TEM. Figure 4 shows TEM micrographs of the A6005-base sample after 6 h of artificial aging. Figure 4a shows two types of precipitates. Those marked with black

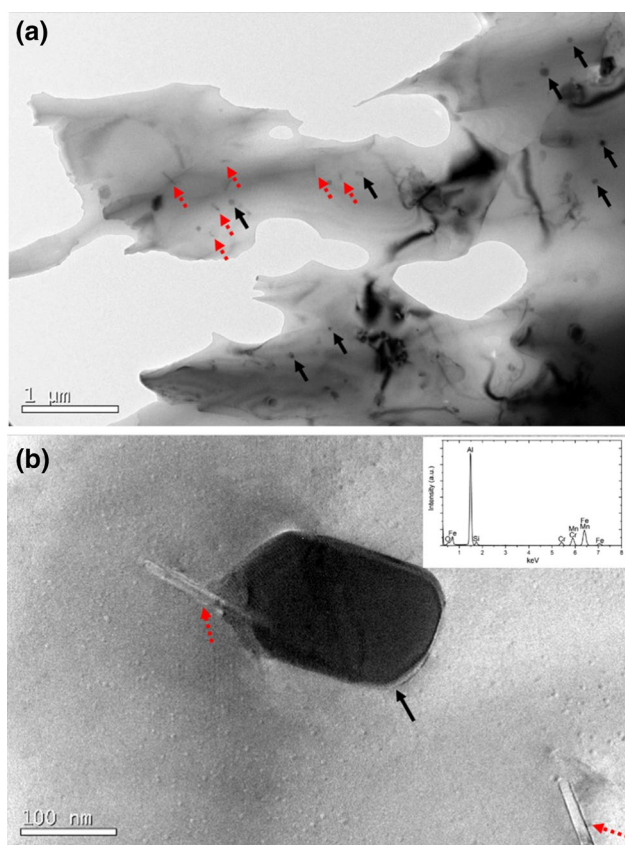


Fig. 4 TEM analysis of A6005-base sample after artificial aging for 6 h: **a** TEM micrograph of the general microstructure and **b** TEM micrograph of α -phase (EDS analysis) and Mg–Si precipitates

arrows are dispersoids with globular morphology and as the EDS spectrum of Fig. 4b revealed, these are formed mainly by iron, presented as the main contaminant in the matrix. Other elements as Si, Mn, and Cr have been also shown in such dispersoids. These dispersoids mainly of the α -Al(Fe,Mn,Cr)Si type are not coherent with the aluminum matrix and present a diameter about a few hundred or fewer nanometers. Lodgaard and Ryum [28] investigated the precipitation of dispersoids containing Mn or Cr in 6xxx alloys and they found that the unit cell of these dispersoids is always SC. In addition, Bayat et al. [29] studied phase transformations during homogenization of 6005 alloy and they concluded that for Mn concentrations between 0.02 and 0.2 wt%, the cubic α type dispersoid is the stable phase. In addition, the presence of Mn also improves the distribution of Mg–Si phase. Couper et al. [30] investigated these dispersoids in 6xxx aluminum alloys and they pointed out that the growth of these dispersoids is controlled by the diffusion of iron to the dispersoids and by substituting with Mn. These dispersoids do not significantly affect the mechanical properties but could cause difficulties during the extrusion, leading to a poor surface finish, hot cracking and defects.

Figure 4 also shows other precipitates with different shape and size marked with dotted red arrows in Fig. 4a. These precipitates are semi-coherent with the matrix and they have rod shape morphology with a length of a few hundred or fewer nanometers. On one hand, the β'' phase has a needle morphology with a monoclinic or hexagonal crystalline structure. This is the predominant precipitate in peak-aged alloys, however, the great size of the precipitates shown by TEM images suggests that they do not correspond with this phase. On the other hand, the β' precipitate is a semi-coherent phase and it has rod shape morphology with a hexagonal structure. This β' phase is the mayor responsible of the strengthening during artificial aging and presumably, the precipitates shown by TEM are this phase. Figure 4b also shows two of these precipitates marked with dotted red arrows. Lodgaard and Ryum [28] studied the nucleation mechanism of the precipitates containing Mn and Cr. They proposed that Mn–Cr containing dispersoids nucleate on Mg–Si β' phase through an intermediate semi-coherent phase called ‘u-phase’. This is an intermediate phase with respect to the α -dispersoid phase which facilitates nucleation event due to the structural similarity. This intermediate phase has not been identified. However, as Fig. 4b shows, Mg–Si and α precipitates nucleate together as Lodgaard and Ryum proposed.

Figure 5 shows TEM images of A6005-MA-5% sample after 5 h of artificial aging. Figure 5a shows the general morphology of the sample and as mentioned before, two clearly differentiated areas have been observed. The EDS analysis performed in point (1) only shown aluminum peaks while in point (2) the EDS also revealed Ti, O, Fe, Mg, and Si peaks. In this area, a higher number of crystals of smaller nanometric size are observed. The presence of Ti peaks means that a greater number of nano-TiB₂ particles are located in this area, while the peak of O implies the formation of Al₂O₃ during the MA. The peaks of Fe have been also shown as in sample A6005-base. The presence of Fe is higher than that in A6005-base sample and it is related to Fe contamination generated during MA process. At higher magnification (Fig. 5b), two particles of approximately 40 nm diameter marked with dotted red arrows have been observed. These particles have been identifying as nano-TiB₂ according to the electron diffraction shown in Fig. 5c, where some of the diffraction rings of TiB₂ have been identified in these crystals. In addition, dispersoids of α -AlFeSi and mainly of α -Al(Fe,Mn,Cr)Si marked with black arrows have been shown in Fig. 5b, as in A6005-base sample. Finally, at higher magnification, fine semi-coherent precipitates of Mg–Si with needle shape and 10 nm length have been shown in Fig. 5d. The reduced size of these precipitates prevented an electron diffraction analysis to identify the phase to which these Mg–Si precipitates corresponded. The size and shape of these precipitates are very similar to

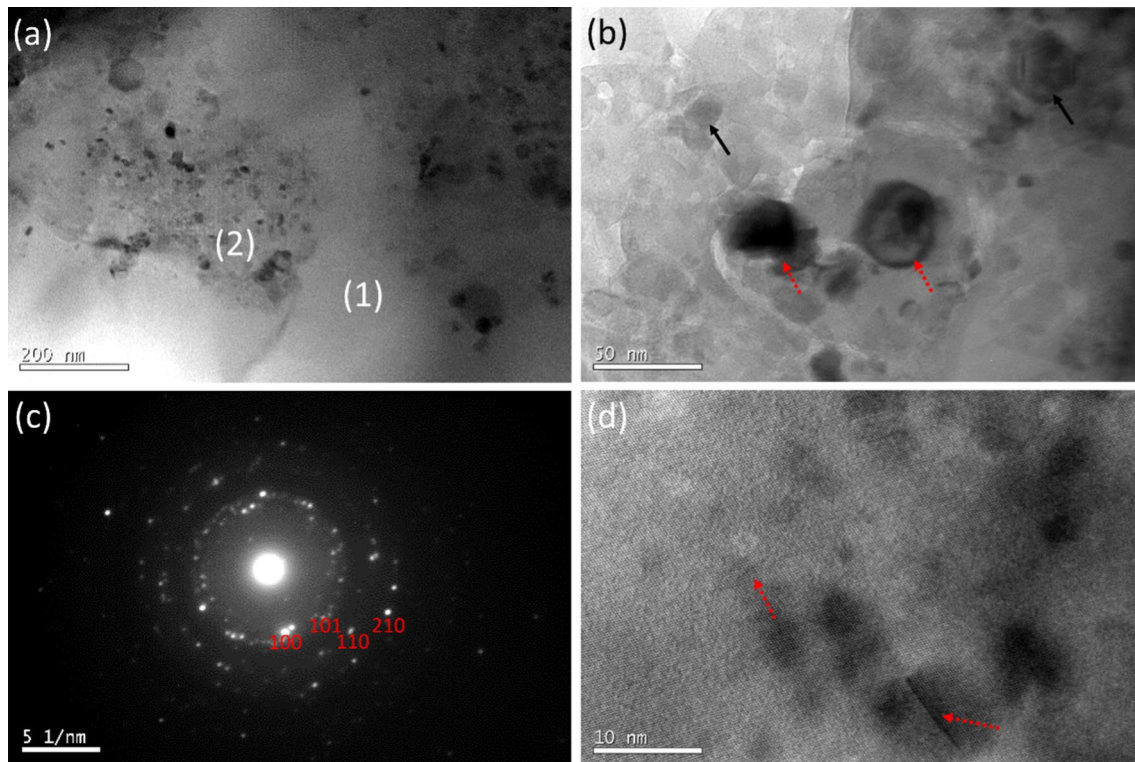


Fig. 5 TEM analysis of A6005-MA-5% material after artificial aging for 5 h: **a** TEM micrograph of the general microstructure, **b** TEM micrograph of n-TiB₂ and α -dispersoids **c** electron diffraction analysis of n-TiB₂ and **d** TEM micrograph of Mg-Si precipitates

that of β' phase. The number of these precipitates was lower than that observed in A6005-base material and therefore on age-hardening plots, the A6005-MA-5% material showed lower increase of micro-hardness.

3.2 Characterization of FSW Joint

A6005-MA-5% plates of 3 mm thickness have been welded by FSW. The heat generated during the friction with the selected parameters has been enough to exceed the flow stress of the composite to produce the joint. The presence of nano-TiB₂ reinforcement supposes higher resistance to beat the flow stress. Kalaiselvan et al. [31] analyzed the effect of B₄C particles on A6061 matrix during the FSW process and they confirmed that the presence of ceramic particles produces more resistance to the free flow of the aluminum matrix. The different zones typically shown in the microstructure of FSW joints have been schematized in Fig. 6. The microstructure is formed by (1) the base material (BM), (2) the heat affected zone (HAZ), (3) the thermo-mechanically affected zone (TMAZ), and (4) the weld zone or nugget. However, in this case the HAZ has not been differentiated by OM from the BM. The other two zones have been differentiated by microstructural changes observed in Fig. 6. The TMAZ is the area that has been affected thermally and

mechanically and suffered plastic deformation. If TMAZ (Fig. 6b) is compared with the BM (Fig. 6a), there is a small reduction of grain size and a change in grains orientation, the TMAZ shows the alignment of the grains in the vertical direction while in the BM, the grains are aligned in the extrusion direction. The TMAZ was clearly identified in the advancing side, however, in the retreating side, it was not revealed. The absence of a boundary at retreating side is due to the plasticized material flow behavior while forging at the back side of the pin, as other authors also observed [31, 32]. The boundary between the TMAZ and the weld zone has been clearly visible. Figure 6c shows the microstructure of the nugget. It suffered severe strain generating a grain refinement. This is indicative of the dynamic recrystallization during the FSW process.

3.3 Precipitation Strengthening of FSW Joint

Cross-sectional aging curves of A6005-FSW sample have been represented in Fig. 7. The as-received FSW has the maximum hardening peak in the nugget zone and the minimum hardening peak in the HAZ. The shape of micro-hardness profile is very common in FSW of AMC joints, as [33, 34] reported. The grain refinement in the nugget zone has been translated into a micro-hardness increase. The

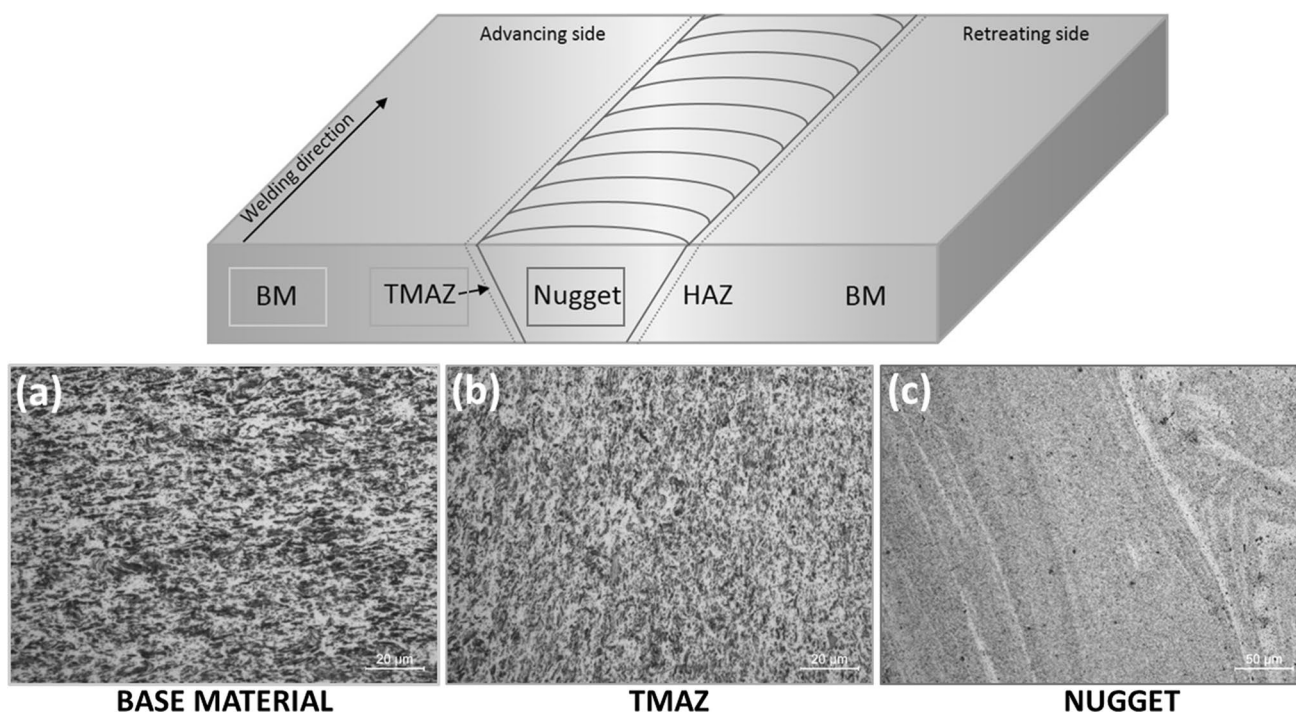


Fig. 6 Scheme of the FSW and optical micrographs of the main zones: **a** base material, **b** thermo-mechanically affected zone and **c** nugget

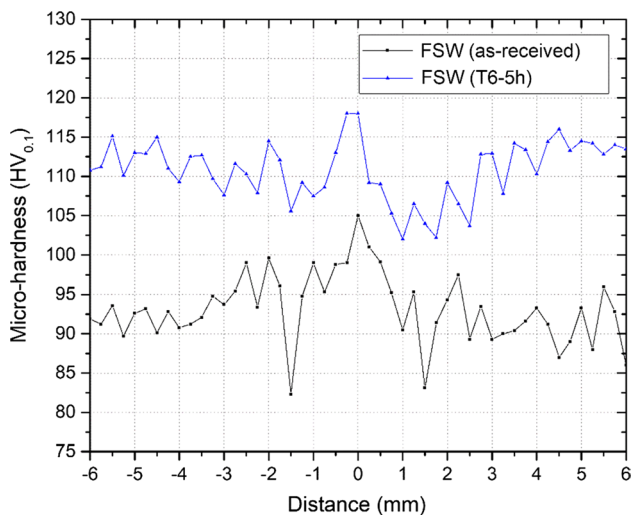


Fig. 7 Micro-hardness profile across the friction stir welded A6005/n-TiB₂ composite

TMAZ has not clearly identified in micro-hardness curve of as-received sample. Otherwise, after T6 thermal treatment (blue plot), the micro-hardness increased significantly in all the joint zones. This suggests that AMCs joints produced by FSW can be thermally treated. After T6 treatment, the maximum micro-hardness peak is still in the nugget zone but this peak is not as marked as in the as-received sample and, as expected, micro-hardness peaks of the HAZ

disappeared after T6 thermal treatment. In this study, the effect of TiB₂ addition has not been evaluated. However, Singh et al. [35] studied the mechanical properties of a FSW A6061-T6 composite reinforced with Al₂O₃ nanoparticles and they obtained micro-hardness values lower than that of our reinforced composite. These authors [6] also studied the same A6061-T6 alloy but reinforced with TiO₂ nanoparticles and they did not achieve micro-hardness values higher than 78 HV in the FSW joint. Again, their maximum micro-hardness was lower than the presented in this research. The comparative results suggest that the combination of both T6 thermal treatment and the addition of TiB₂ nanoparticles in the A6005 alloy would greatly improve the final properties of the welded material.

3.4 Effect of FSW Process on Corrosion Behavior

The effect of the FSW process on corrosion behavior has been evaluated by electrochemical tests. A6005-MA-5% and A6005-FSW materials, both in T6 condition, have been used for this propose. Linear polarization tests have been first performed to evaluate the effect of corrosion products on the electrochemical process. The corrosion potential (OCP) versus time is shown in Fig. 8a. Both samples showed that even with longer immersion times, the steady state potential has been maintained, suggesting an effective stabilization of the Al₂O₃ passive film. The steady state potential was achieved

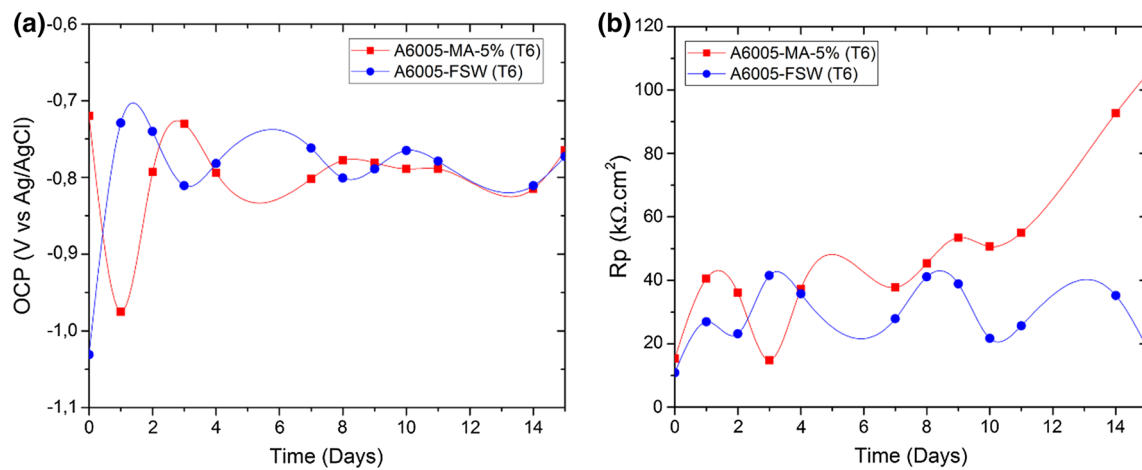


Fig. 8 Linear polarization tests in 3.5 wt% NaCl solution: **a** open circuit potential OCP versus time and **b** polarization resistance R_p versus time

in both samples after approximately 2 days of immersion. This stable anodic behavior is due to the Al_2O_3 presence.

In addition, as Fig. 8b shows, in both samples R_p did not decrease over time, due to the presence of the Al_2O_3 passive film which blocks the corrosion process. After 1 h

immersion R_p values were around 15–20 $k\Omega/cm^2$ in both samples. After this hour, the formation of the Al_2O_3 passive film produced an increase of R_p values. This behavior stands out in the A6005-MA-5% material, where the upward trend has been maintained up to the end of the

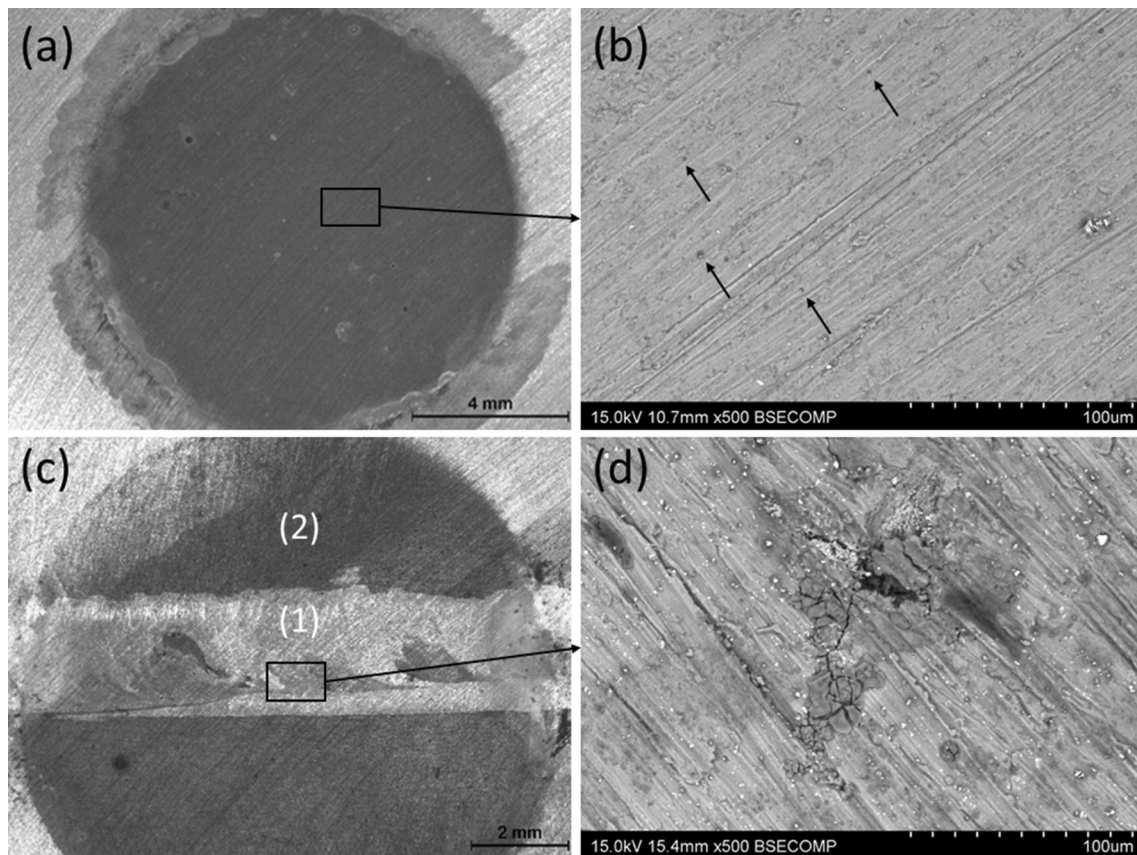


Fig. 9 Macro and micrographs of the surface of samples exposed to 3.5 wt% NaCl solution after 15 days: **a–b** A6005-MA-5% and **c–d** A6005-FSW samples

test. As Fig. 9a shows, the passive film of A6005-MA-5% sample presents a dark appearance and it is distributed homogeneously along the exposed surface, providing protection capacity. Due to this, R_p increased with time up to the end of the test. The EDX analyses (not shown in Fig. 9) carried out in these areas revealed that Al and O are the major elements. This confirmed the generation of a protective layer of Al_2O_3 . In some specific areas of the surface, this Al_2O_3 layer was covered by aluminum hydroxide ($Al_2O_3 \cdot 3H_2O$). Figure 9b shows SEM micrograph of representative pits (marked with black arrows) produced by the penetration of chloride ions through the passive film. These pits of few micrometers has a circular shape and are distributed homogeneously through the surface. The EDX performed on these pits at higher magnification (not shown in Fig. 9) shown the presence of iron. This suggests that these pits nucleate on Fe-rich zones due to the formation of galvanic couples between the matrix and Fe contaminants.

Otherwise, A6005-FSW sample had worse behavior than A6005-MA-5% and R_p did not increase with time. This is because Al_2O_3 film does not have the same protection capacity and therefore fluctuations of R_p are observed. As Fig. 9c shows, the welded area of A6005-FSW sample (area 1) does not have a layer of dark products while the base material has it (area 2). The absence of this passive layer on the welded zone is probably associated with a change in the E_{corr} between the base material and the joint. This difference can be attributed to microstructural changes that could generate galvanic corrosion due to an increase of the deformation and therefore of the residual stress presented in the welded zone. At higher magnification, pits, as well as corrosion products, have been analyzed in detail. Similar pits to that of A6005-MA-5% sample have been observed in the base material (not shown in Fig. 9). However, in the weld zone (Fig. 9d), higher pits with irregular morphology have been observed. The huge size of this pits (tens of micrometers) in the welded zone suggests that this area is more susceptible to suffer pitting corrosion by the formation of galvanic couples, with Fe contaminants and nano- TiB_2 reinforcement, due to the absence of the protective passive layer.

Figure 10 shows the anodic–cathodic polarization plots after 1 h and 360 h immersion. The OCP and the corrosion current density (i_{corr}) are summarized in Table 2. It shows how i_{corr} increases with immersion time, raising from 0.05 to 0.58 $\mu A/cm^2$ for the A6005-MA-5% sample and from 0.16 to 2.50 $\mu A/cm^2$ for the A6005-FSW sample. The A6005-MA-5% sample exhibits higher corrosion resistance in the 3.5 wt% NaCl solution compared to the A6005-FSW sample.

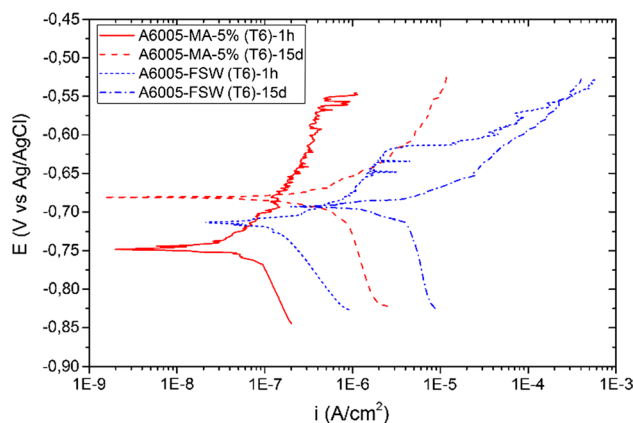


Fig. 10 Polarization plots of A6005-MA-5% and A6005-FSW samples after 1 h and 360 h immersion in 3.5 wt% NaCl solution

Table 2 Corrosion current densities (i_{corr}) of A6005-MA-5% and A6005-FSW samples at different immersion times

Sample	Immersion time (h)	E_{corr} (V)	i_{corr} ($\mu A/cm^2$)
A6005-MA-5%	1	-0.748	0.05
	360	-0.681	0.58
A6005-FSW	1	-0.713	0.16
	360	-0.693	2.50

4 Conclusions

- The precipitation sequence of the A6005/nano- TiB_2 composite has been approximated to the following sequence: $\alpha Al + \text{clusters of Si and Mg} \rightarrow \alpha Al + GP \text{ zones} \rightarrow \alpha Al + \beta'' \rightarrow \alpha Al + \beta' \rightarrow \alpha Al + \beta (Mg_2Si)$.
- TiB_2 reinforcement acts as a nucleation site and probably accelerates precipitation kinetic of β' and β hardening phases. In addition, samples processed by MA route, with and without reinforcement, have less susceptible to T6 thermal treatment.
- TEM characterization revealed two main precipitates embedded in the aluminum matrix: $\alpha-Al(FeMnCr)Si$ dispersoids with globular morphology and the Mg–Si hardening phase with needle morphology, associated with the β' phase.
- Three different areas -the BM, the TMAZ, and the weld zone- have been distinguished in the FSW and the mechanical properties of the FSW have been improved after T6 thermal treatment. The maximum micro-hardness has been obtained in the weld zone due to grain refinement.
- The welded sample had more susceptible to suffer pitting corrosion due to the formation of galvanic couples

with Fe contaminants and to the absence of the Al_2O_3 passive layer in the weld zone.

- The welded sample had less corrosion resistance in the 3.5 wt% NaCl solution than the unjoined sample as corrosion current density values reported.

Acknowledgements This research has been conducted with the economic support of Ministerio de Economía y Competitividad (MAT2013-48166-C3-3-R) and Comunidad de Madrid (ADITIMAT-CM, S2018/NMT-4411).

References

1. A. Wagih, Mechanical properties of Al–Mg/ Al_2O_3 nanocomposite powder produced by mechanical alloying. *Adv. Powder Technol.* **26**, 253–258 (2015). <https://doi.org/10.1016/j.apt.2014.10.005>
2. I. Dinaharan, N. Murugan, Optimization of friction stir welding process to maximize tensile strength of AA6061/ZrB₂ in-situ composite butt joints. *Met. Mater. Int.* **18**, 135–142 (2012). <https://doi.org/10.1007/s12540-012-0016-z>
3. A.R. Othman, A. Sardarinejad, A.K. Masrom, Effect of milling parameters on mechanical alloying of aluminum powders. *Int. J. Adv. Manuf. Technol.* **76**, 1319–1332 (2014). <https://doi.org/10.1007/s00170-014-6283-8>
4. I. Feijoo, M. Cabeza, P. Merino et al., Estimation of crystallite size and lattice strain in nano-sized TiC particle-reinforced 6005A aluminium alloy from X-ray diffraction line broadening. *Powder Technol.* **343**, 19–28 (2019). <https://doi.org/10.1016/j.powtec.2018.11.010>
5. N. Abu-Warda, M.V. Utrilla, M.D. Escalera et al., The effect of TiB₂ content on the properties of AA6005/TiB₂ nanocomposites fabricated by mechanical alloying method. *Powder Technol.* (2018). <https://doi.org/10.1016/j.powtec.2018.01.028>
6. T. Singh, S.K. Tiwari, D.K. Shukla, Mechanical and microstructural characterization of friction stir welded AA6061-T6 joints reinforced with nano-sized particles. *Mater. Charact.* **159**, 110047 (2020). <https://doi.org/10.1016/j.matchar.2019.110047>
7. S. Babu, K. Elangovan, V. Balasubramanian, M. Balasubramanian, Optimizing friction stir welding parameters to maximize tensile strength of AA2219 aluminum alloy joints. *Met. Mater. Int.* **15**, 321–330 (2009). <https://doi.org/10.1007/s12540-009-0321-3>
8. L. Wan, Y. Huang, W. Guo et al., Mechanical properties and microstructure of 6082-T6 aluminum alloy joints by self-support friction stir welding. *J. Mater. Sci. Technol.* **30**, 1243–1250 (2014). <https://doi.org/10.1016/j.jmst.2014.04.009>
9. J. Dong, D. Zhang, W. Zhang et al., Microstructure and properties of underwater friction stir-welded 7003-T4/6060-T4 aluminum alloys. *J. Mater. Sci.* **54**, 11254–11262 (2019). <https://doi.org/10.1007/s10853-019-03676-5>
10. T. Chen, Process parameters study on FSW joint of dissimilar metals for aluminum-steel. *J. Mater. Sci.* **44**, 2573–2580 (2009). <https://doi.org/10.1007/s10853-009-3336-8>
11. Y. Birol, Precipitation during homogenization cooling in AlMgSi alloys. *Trans. Nonferrous Met. Soc. China* **23**, 1875–1881 (2013). [https://doi.org/10.1016/S1003-6326\(13\)62672-2](https://doi.org/10.1016/S1003-6326(13)62672-2)
12. W. Yang, S. Ji, Z. Li, M. Wang, Grain boundary precipitation induced by grain crystallographic misorientations in an extruded Al–Mg–Si–Cu alloy. *J. Alloys Compd.* **624**, 27–30 (2015). <https://doi.org/10.1016/j.jallcom.2014.10.206>
13. G.A. Edwards, K. Stiller, G.L. Dunlop, M.J. Couper, The precipitation sequence in Al–Mg–Si alloys. *Acta Mater.* **46**, 3893–3904 (1998). [https://doi.org/10.1016/S1359-6454\(98\)00059-7](https://doi.org/10.1016/S1359-6454(98)00059-7)
14. A. Schiffl, S. Schwarz, G.R. Bourret et al., Secondary precipitation during homogenization of Al–Mg–Si alloys: influence on high temperature flow stress. *Mater. Sci. Eng. A* **687**, 175–180 (2017). <https://doi.org/10.1016/j.msea.2017.01.074>
15. P. Rodrigo, P. Poza, V. Utrilla, A. Ureña, Effect of reinforcement geometry on precipitation kinetics of powder metallurgy AA2009/SiC composites. *J. Alloys Compd.* **479**, 451–456 (2009). <https://doi.org/10.1016/j.jallcom.2008.12.114>
16. O.S. Salih, H. Ou, W. Sun, D.G. McCartney, A review of friction stir welding of aluminium matrix composites. *Mater. Des.* **86**, 61–71 (2015). <https://doi.org/10.1016/j.matdes.2015.07.071>
17. Y.C. Chen, J.C. Feng, H.J. Liu, Precipitate evolution in friction stir welding of 2219-T6 aluminum alloys. *Mater. Charact.* **60**, 476–481 (2009). <https://doi.org/10.1016/j.matchar.2008.12.002>
18. K. Elangovan, V. Balasubramanian, Influences of post-weld heat treatment on tensile properties of friction stir-welded AA6061 aluminum alloy joints. *Mater. Charact.* **59**, 1168–1177 (2008). <https://doi.org/10.1016/j.matchar.2007.09.006>
19. M. Navaser, M. Atapour, Effect of friction stir processing on pitting corrosion and intergranular attack of 7075 aluminum alloy. *J. Mater. Sci. Technol.* **33**, 155–165 (2017). <https://doi.org/10.1016/j.jmst.2016.07.008>
20. B. Seo, K. Hyun, S. Kwangsuk, Corrosion properties of dissimilar friction stir welded 6061 aluminum and HT590 steel. *Met. Mater. Int.* (2018). <https://doi.org/10.1007/s12540-018-0135-2>
21. S. Maggiolino, C. Schmid, Corrosion resistance in FSW and in MIG welding techniques of AA6XXX. *J. Mater. Process. Technol.* **197**, 237–240 (2008). <https://doi.org/10.1016/j.jmatp.2007.06.034>
22. N. Abu-Warda, M.D. López, M.D. Escalera-Rodríguez et al., Corrosion behavior of mechanically alloyed A6005 aluminum alloy composite reinforced with TiB₂ nanoparticles. *Mater. Corros.* (2019). <https://doi.org/10.1002/maco.201911174>
23. M. Cabeza, I. Feijoo, P. Merino et al., Effect of high energy ball milling on the morphology, microstructure and properties of nano-sized TiC particle-reinforced 6005A aluminium alloy matrix composite. *Powder Technol.* **321**, 31–43 (2017). <https://doi.org/10.1016/j.powtec.2017.07.089>
24. Y. Weng, Z. Jia, L. Ding et al., Clustering behavior during natural aging and artificial aging in Al–Mg–Si alloys with different Ag and Cu addition. *Mater. Sci. Eng. A* **732**, 273–283 (2018). <https://doi.org/10.1016/j.msea.2018.07.018>
25. A. Serizawa, S. Hirose, T. Sato, Three-dimensional atom probe characterization of nanoclusters responsible for multistep aging behavior of an Al–Mg–Si alloy. *Met. Mater. Trans. A* **39**, 243–251 (2008)
26. C.D. Marioara, S.J. Andersen, J. Jansen, H.W. Zandbergen, Atomic model for GP-zones in a 6082 Al–Mg–Si system. *Acta Mater.* **49**, 321–328 (2001). [https://doi.org/10.1016/S1359-6454\(00\)00302-5](https://doi.org/10.1016/S1359-6454(00)00302-5)
27. Y. Birol, DSC analysis of the precipitation reaction in AA6005 alloy. *J. Therm. Anal. Calorim.* **93**, 977–981 (2008). <https://doi.org/10.1007/s10973-007-8686-3>
28. L. Lodgaard, N. Ryum, Precipitation of dispersoids containing Mn and/or Cr in Al–Mg–Si alloys. *Mater. Sci. Eng.* **283**, 144–152 (2000)
29. N. Bayat, T. Carlberg, M. Cieslar, In-situ study of phase transformations during homogenization of 6005 and 6082 Al alloys. *J. Alloys Compd.* **725**, 504–509 (2017). <https://doi.org/10.1016/j.jallcom.2017.07.149>
30. M. Couper, K. Strobel, J.F. Nie et al., Dispersoid phases in 6xxx series aluminium alloys. *Mater. Sci. Forum* **654–656**,

- 926–929 (2010). <https://doi.org/10.4028/www.scientific.net/msf.654-656.926>
31. K. Kalaiselvan, I. Dinaharan, N. Murugan, Characterization of friction stir welded boron carbide particulate reinforced AA6061 aluminum alloy stir cast composite. *Mater. Des.* **55**, 176–182 (2014). <https://doi.org/10.1016/j.matdes.2013.09.067>
 32. X.G. Chen, M. da Silva, P. Gougeon, L. St-Georges, Microstructure and mechanical properties of friction stir welded AA6063-B4C metal matrix composites. *Mater. Sci. Eng. A* **518**, 174–184 (2009). <https://doi.org/10.1016/j.msea.2009.04.052>
 33. D. Wang, Q.Z. Wang, B.L. Xiao, Z.Y. Ma, Achieving friction stir welded SiCp/Al–Cu–Mg composite joint of nearly equal strength to base material at high welding speed. *Mater. Sci. Eng. A* **589**, 271–274 (2014). <https://doi.org/10.1016/j.msea.2013.09.096>
 34. D. Verdera, R. Fernández, F. Cioffi et al., Friction stir welding of thick plates of aluminum alloy matrix composite with a high volume fraction of ceramic reinforcement. *Compos. Part A Appl. Sci. Manuf.* **54**, 117–123 (2013). <https://doi.org/10.1016/j.compositesa.2013.07.011>
 35. T. Singh, S.K. Tiwari, D.K. Shukla, Friction-stir welding of AA6061-T6: the effects of Al₂O₃ nano-particles addition. *Results Mater.* **1**, 100005 (2019). <https://doi.org/10.1016/j.rinma.2019.100005>

Publisher's Note Springer Nature remains neutral with regard to jurisdictional claims in published maps and institutional affiliations.